Label-free imaging of drug distribution and metabolism in colon cancer cells by Raman microscopy†

Samir F. El-Mashtoly,[a] Dennis Petersen,[a] Hesham K. Yosef,[a] Axel Mosig,[a] Anke Reinacher-Schick,[b] Carsten Kötting[a] and Klaus Gerwert*[a]

Targeted cancer therapies block cancer growth and spread using small molecules. Many molecular targets for an epidermal growth factor receptor (EGFR) selectively compete with the adenosine triphosphate-binding site of its tyrosine kinase domain. Detection of molecular targeted agents and their metabolites in cells/tissues by label-free imaging is attractive because dyes or fluorescent labels may be toxic or invasive. Here, label-free Raman microscopy is applied to show the spatial distribution of the molecular targeted drug erlotinib within the cell. The Raman images show that the drug is clustered at the EGFR protein at the membrane and induces receptor internalization. The changes within the Raman spectrum of erlotinib measured in cells as compared to the free-erlotinib spectrum indicate that erlotinib is metabolized within cells to its demethylated derivative. This study provides detailed insights into the drug targeting mechanism at the atomic level in cells. It demonstrates that Raman microscopy will open avenues as a non-invasive and label-free technique to investigate pharmacokinetics at the highest possible resolution in living cells.

Introduction

In drug discovery and development, the uptake and distribution of a drug candidate in targeted cells/tissues are pivotal for the evaluation of its pharmaceutical properties. Important information related to the absorption, distribution, metabolism, and excretion of drugs, such as accumulation at the level of the targeted cell/tissue, is also desired. The distribution of pharmaceutical compounds inside cells/tissues has been investigated using several techniques such as positron emission tomography, magnetic resonance imaging, and whole body autoradiography.[1–3] These techniques may be applied *in vivo*; however, the major limitations include the requirement of radioactive isotope labeling or the use of a reporter molecule. In recent years, there has been growing interest in applying label-free imaging methods such as matrix-assisted laser desorption ionization with mass spectrometry (MALDI-MS) to the analysis of pharmaceutical compounds and their metabolites in biological tissue sections.[4–7] However, this method can be applied only to low molecular weight compounds and suffers from a low spatial resolution of approximately 20 μm. All the above methods suffer from either low sensitivity and/or low spatial resolution. On the other hand, Raman microspectroscopy is a non-invasive and label-free method to assess and image cellular processes based on their biochemical changes without further sample preparation.[8–14] Raman microspectroscopy affords high sensitivity to small intracellular fluctuations as well as a high spatial resolution of approximately 0.5 μm. This technique is based on the identification of molecular vibrations that are distinct for all major species in cells and tissues such as proteins, nucleic acids, lipids, phospholipids, and carbohydrates as well as a variety of molecules such as drugs or metabolites. Raman microscopy has been used to image cellular organelles[8–13,15] and also to follow the uptake of liposomal drug carrier systems[16–18] and alkyne-tagged proliferation probes.[19] In addition, the distribution of chemotherapeutic drugs in cells has been reported.[20–24] However, the cellular uptake of these drugs in the cell culture occurred without carrier systems. The distribution and metabolism of the molecular targeted agent using a carrier system will be discussed in the present study.

Targeted cancer therapies have been directed towards cancer-specific molecules and signaling pathways.[25–27] Some targeted agents have high selectivity and potency, are less harmful to normal cells, and have reduced side effects, and thus may be more effective than chemotherapy. Tyrosine kinase receptors are important targets because they play a vital role in the modulation of growth factor signaling, and their activated

[a] *Department of Biophysics, Ruhr-University Bochum, 44780 Bochum, Germany. E-mail: gerwert@bph.ruhr-uni-bochum.de; Fax: +49-(0)234-3214238; Tel: +49-(0)234-3224461*

[b] *Department of Hematology and Oncology, St. Josef-Hospital, Ruhr-University Bochum, Bochum, Germany*

forms can induce an increase in cancer cell proliferation and growth. Tyrosine kinases catalyze the transfer of the terminal phosphate group from adenosine triphosphate (ATP) to target proteins that contain tyrosine residues.[28–30]

Inhibitors of tyrosine kinase receptors are selective small molecules and compete with the ATP binding site of their tyrosine kinase domain, and their pharmacokinetics are not fully understood.[31] Several inhibitors of tyrosine kinase have been found to exhibit anti-tumor activity and have been approved by the United States Food and Drug Administration (FDA) and European Medicines Agency.[32] For instance, erlotinib (Tarceva) is an epidermal growth factor receptor (EGFR) inhibitor approved for the treatment of locally advanced or metastatic non-small cell lung and pancreatic cancers.[33] Erlotinib is also used in clinical trials to treat colon cancer. EGFR is over-expressed in several tumors, such as those of the breast, head and neck, lung, bladder, colon, cervix, kidney, and brain, and it is one of the main strategic target for systematic therapy.[34,35]

Here, we investigate the uptake, distribution, and metabolism of erlotinib in colon cancer cells by Raman microscopy. Erlotinib shows a strong signal due to the acetylene (C≡C) stretching that can be used as a label-free marker for imaging this drug or its metabolite in cells. Furthermore, the results indicated that erlotinib is internalized and metabolized to its demethylated derivative in colon cancer cells.

Experimental

Cell culture

Human colorectal adenocarcinoma SW480 (CCL-228) cells were obtained from the American Type Culture Collection. The cells were grown in Dulbecco's modified Eagle's medium (DMEM, Invitrogen, Carlsbad, USA) supplemented with 10% fetal bovine serum (FBS, Invitrogen, Carlsbad, USA), 2 mM L-glutamine, and 5% penicillin–streptomycin and incubated at 37 °C in 5% CO_2 atmosphere. Cells were regularly subcultured when they reached ∼80% confluence with 0.25% trypsin–EDTA. Raman data were acquired on cells grown on CaF_2 windows (Korth Kristalle, Kiel, Germany) to avoid background signals from the regular glass slides. Cells were grown under these normal conditions and also were synchronized in G_0 by serum starvation, where the FBS-containing medium was removed and cells were cultured on a starving medium (0.1% FBS) containing 2 mM L-glutamine for 24 hours. Cells were not so stressed under serum starvation conditions (see Fig. S1 in the ESI†). Cells were incubated with erlotinib (∼100 μM) at 37 °C in 5% CO_2 for 12 hours. Afterwards, cells were fixed in 4% paraformaldehyde (VWR International, Darmstadt, Germany) and subsequently submerged into the phosphate-buffered saline (PBS; Invitrogen, Carlsbad, USA).

Confocal Raman microscopy

Raman microspectroscopy was acquired using a WITec alpha 300AR confocal Raman microscope (Ulm, Germany) as described in detail previously.[36] Briefly, a frequency-doubled Nd:YAG laser operating at 532 nm (Crystal laser, Reno, USA) was used as an excitation source with the output power around 40 mW. The exciting laser radiation was coupled into a Zeiss microscope through a wavelength-specific single-mode optical fiber with a diameter of 25 μm. The incident laser beam was collimated *via* an achromatic lens and passed through a holographic band-pass filter before being focused into the sample through a Nikon NIR APO (60×/1.00 NA) water immersion objective. The sample was located on a piezoelectrically driven microscope scanning stage, which had an x, y resolution of 3 nm, a reproducibility of ±5 nm and a z resolution of 0.3 nm with a repeatability of ±2 nm. Raman back-scattered light was collected through a microscopic objective and passed through a holographic edge filter onto a multimode fiber (50 μm diameter) and into a 300 mm focal length monochromator incorporating a 600 mm^{-1} grating blazed at 500 nm. Detection of Raman spectra was provided by a back-illuminated deep-depletion charge coupled device (CCD) camera operating at −60 °C.

Imaging experiments were performed by raster-scanning the laser beam over cells and accumulating a full Raman spectrum at each pixel at a speed of 0.5 s/pixel. The image size is in the range of 170 × 170 pixels and 85 × 85 μm, depending on the shape and size of the cells studied. Raman images were constructed by integrating over the C–H vibrational bands at 2800–3050 cm^{-1}.

Fluorescence microscopy

CaF_2 windows used previously in the Raman measurements were used for immunofluorescence imaging. First, the formalin-fixed cells were permeabilized with 0.2% Triton X-100 for 5 minutes at room temperature. After washing with PBS, cells were blocked with 1% bovine serum albumin (BSA) for 30 minutes. The cells were incubated with the primary rabbit monoclonal anti-EGFR (D38B1; Cell Signaling Technology, Danvers, USA) overnight at 4 °C followed by washing with the PBS buffer and incubation for 1 hour with the secondary antibody conjugated with tetramethyl rhodamine isothiocyanate (TRITC; Jackson ImmunoResearch, West Grove, USA), at room temperature. Excess antibodies were removed by washing three times with the PBS buffer. Cells were incubated with 1,5-bis{[2-(di-methylamino) ethyl]amino}-4,8-dihydroxyanthracene-9,10-dione (DRAQ-5; Cell Signaling Technology, Danvers, USA) for 10 minutes followed by washing with the PBS buffer.

Fluorescence measurements were performed with a confocal laser scanning microscope (Leica TCS SP5 II) using a Leica HCX PL APO (63×/1.4 NA) oil immersion objective. Nucleus and EGFR fluorescence was imaged sequentially by exciting with the 633 nm red helium–neon and 561 nm diode-pumped solid state lasers, respectively.

Multivariate analysis

The Raman spectra of cells were analyzed using an unsupervised learning algorithm, hierarchical cluster analysis (HCA). All data were imported into the Matlab 7.13 software package (R2011b; MathWorks Inc., MA) and data preprocessing and the multivariate analysis were implemented using in-house built scripts. Spectra which had no C–H band at 2850–3000 cm^{-1} were considered as the background and were deleted. Peaks caused by cosmic rays were removed. Afterwards, all spectra were

baseline corrected using a 3rd order polynomial and were also vector normalized. HCA on the regions of 700–1800 and 2800–3050 cm^{-1} using Ward's clustering in combination with Pearson correlation distance was found to produce the best clustering as judged by the homogeneity of the spectra in each cluster.

Quantum chemical calculations

The geometry of the fragments shown in Fig. S2 (see the ESI†) was optimized at the B3LYP/6-31G(d) level of theory using the gaussian03 program package. The water environment was simulated by the Onsager model with the dielectric constant $\varepsilon = 78.39$. Vibrational frequencies were calculated analytically and non-resonant Raman intensities were obtained from the polarizability derivatives. No scaling factor was applied.

Results and discussion

Label-free Raman imaging of erlotinib in colon cancer cells

In the present study, we follow the uptake of the molecular targeted agent erlotinib to its site of action, the tyrosine kinase domain of EGFR, within colon cancer cells (SW480). To improve the solubility of erlotinib in cell culture and facilitate its delivery, it was dissolved in 6% captisol in water. Captisol is a polyanionic β-cyclodextrin derivative modified by a sulfobutylether. In addition, captisol has an excellent clinical safety record and is currently used as a safe drug carrier in several FDA approved drugs.[37] Erlotinib is also given to the patients orally in combination with captisol. Fig. 1 shows the Raman microspectroscopic results for SW480 cells incubated for 12 hours with approximately 100 μM (∼50 mg kg^{-1}) erlotinib. At this concentration, most of the cells are viable, as indicated by the cytotoxicity assay (see Fig. S3 in the ESI†). It is a colorimetric assay used for measuring the activity of mitochondria and it reflects the number of the present viable cells. The concentration we used in the present study is at least 10 times lower than that used for Raman imaging of a drug candidate for cancer therapy in a recent study[24] and is similar to the concentrations used for *in vivo* studies of mice.[38] SW480 cells have a characteristic shape and size, typically between 15 and 20 μm in diameter. Fig. 1A depicts the integrated Raman intensity of the C–H stretching region (2800 to 3050 cm^{-1}), reflecting the different densities of various cellular components. Clearly discernible is the nucleus with distinct nucleoli, surrounded by the cytoplasm. Panel B displays the integrated Raman intensity of the C≡C (2085 to 2140 cm^{-1}) stretching vibrations for the same cells. The C≡C stretching vibrations occur in a Raman silent region of cells (1800 to 2800 cm^{-1}) and are used as a label-free marker for erlotinib. It appears that after 12 hours of incubation with erlotinib, some of it gets associated with the cells. Panel C shows an overlay of C–H (panel A) and C≡C (panel B) intensities, indicating that erlotinib is distributed in the cell periphery.

The feasibility of using Raman microscopy coupled with multivariate analyses to visualize cellular and tissue components has been demonstrated.[39,40] In the present study, we have computed HCA of a Raman dataset and the results are shown in panel D. HCA determines the similarity of the spectra within the
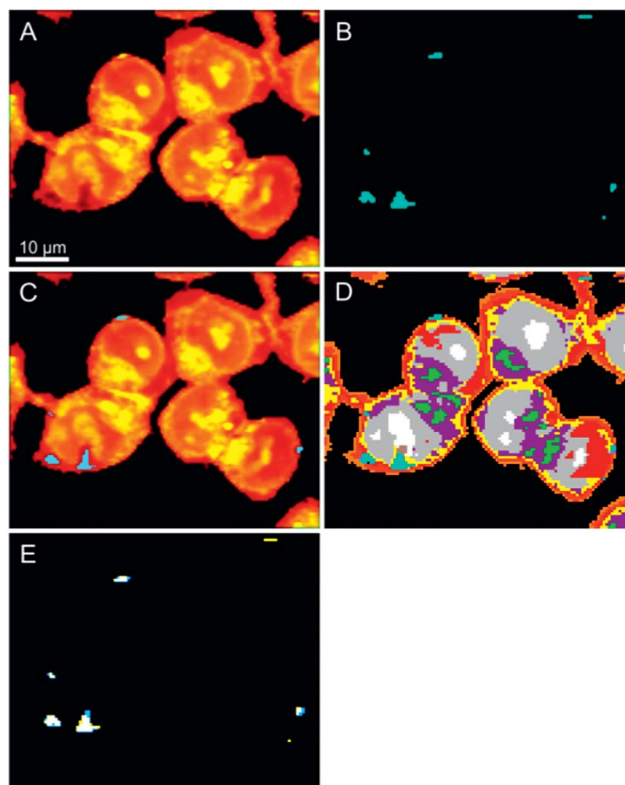

Fig. 1 Raman imaging of SW480 cells treated with approximately 100 μM erlotinib for 12 hours. (A) Raman image reconstructed from the C–H stretching intensity. (B) Raman image reconstructed from C≡C stretching intensity. (C) Overlay of panels (A) and (B). (D) HCA results based on the Raman data shown in (A). (E) Overlay of (B) in cyan with the erlotinib cluster from (D) in pale yellow.

dataset by calculating the correlation distance of each single spectrum with every other spectrum in the same dataset. The most similar spectra are grouped together into separate clusters and each cluster is assigned a colour.[39–41] The clustering was performed in the spectral range of 700 to 1800 and 2800 to 3100 cm^{-1}. This region exhibits most predominant bands of amino acids, protein backbones, nucleotides, nucleic acid backbones, carbohydrates and lipids; it contains sufficient spectral information to give the best clustering results. Eleven clusters were chosen to contrast the drug in one cluster. The clustering reproduces the position of the nucleus with nucleoli, as well as several regions within the cytoplasm, reflecting different compositions of the cytoplasm with various subcellular components. In addition, the spectrum of one cluster (shown in cyan) shows most of the features of the erlotinib spectrum, including the signal of the C≡C band, while this band is absent in all other clusters (see below). Thus, HCA was able to detect the drug in a cluster separate from other cellular components.

Furthermore, we have compared HCA results with other multivariate methods such as multivariate curve resolution-alternating least squares, vertex component analysis, and principle component analysis of the Raman dataset (Fig. 1) and the results are shown in Fig. S4 (see the ESI†). All methods allocate the drug at the same positions in cells but HCA satisfactorily visualizes several cellular components.

To confirm that erlotinib is not precipitated on the surface of cells, we performed three-dimensional Raman imaging (see Fig. S5 in the ESI†) and the results clearly demonstrate that the drug is accumulated inside cells. This is because the univariate Raman maps (Fig. S5†) were collected ∼3–5 μm above the interface between cells and the CaF$_2$ window, where the cell thickness was around 10 μm. Thus, we demonstrate that the C≡C vibrations can be used as a label-free marker for imaging this drug in colon cancer cells. Raman imaging of molecules containing C≡C vibrations such as the alkyne-tagged cell proliferation probe in cells has been reported,[19] but the uptake of this compound into cells occurred without using any carrier system. On the other hand, erlotinib in the present study is delivered into cells through a captisol carrier.

Detection of an erlotinib metabolite

The spectrum in Fig. 2a represents an average spectrum of the cytoplasm and nucleus, where no erlotinib is located.

The most pronounced Raman bands result from the C–H stretching vibrations between 2800 and 3050 cm^{-1}, the carbonyl stretching (amide I) located around 1658 cm^{-1}, C–H and CH$_2$ bending deformation at 1449 cm^{-1}, amide III of the peptide linkages between 1200 and 1400 cm^{-1}, and the ring-breathing

mode of phenylalanine at 1006 cm^{-1}.[9] An average spectrum of the erlotinib region (Fig. 1B) is shown in Fig. 2b.

The intensity of the C≡C vibrations is well pronounced between 1950 and 2150 cm^{-1} and appears at the same spectral positions for free erlotinib (Fig. 2c) as well as for erlotinib in cells (Fig. 2b). It is also noteworthy that the observed erlotinib in cells (Fig. 1B) is free from its carrier captisol as indicated by the absence of the Raman band at 1053 cm^{-1}, a marker for captisol (see Fig. S6 in the ESI†). This is based on the presence of the 1053 cm^{-1} band only in the spectrum of captisol but not in the erlotinib spectrum. Additionally, the spectrum of erlotinib most likely contains contributions from cells, as indicated by Raman bands mainly located at 2935 cm^{-1} (lipid) and 1658 cm^{-1} (protein). Furthermore, the spectrum of erlotinib in cells (Fig. 2b) is significantly different from that of free erlotinib (Fig. 2c) especially in the 1170 to 1595 cm^{-1} region. These results suggest that erlotinib is metabolized. Note that we have only observed the distribution of the metabolite of erlotinib but an intact form of erlotinib was not detected under the current experimental conditions. Thus, the results show the potential of Raman microscopy for the detection of drug metabolites.

Internalization of EGFR induced by erlotinib

Fluorescence microscopy is the most common method to visualize the distribution of proteins in cells.[42] To examine the intracellular distribution of EGFR in SW480 cells, cells were labeled with antibodies specific to EGFR in the absence and presence of erlotinib and fluorescence measurements were performed (Fig. 3). As expected, most of the EGFR was associated with the plasma membrane (panel A). However, in the presence of erlotinib, a fraction of the EGFR was clustered in cells (panel B). This may lead to an increase in the local concentration of erlotinib at the clustered regions of the EGFR, and therefore, erlotinib can be detected using the present Raman measurements. It is noted that most of cells treated by erlotinib are round (panel B). This is probably caused by erlotinib, which induces apoptosis and cell cycle arrest.[43–46] It is reported that cetuximab, a monoclonal anti-EGFR antibody, promotes EGFR internalization without receptor phosphorylation and inhibits the cell proliferation.[47–49] Because no
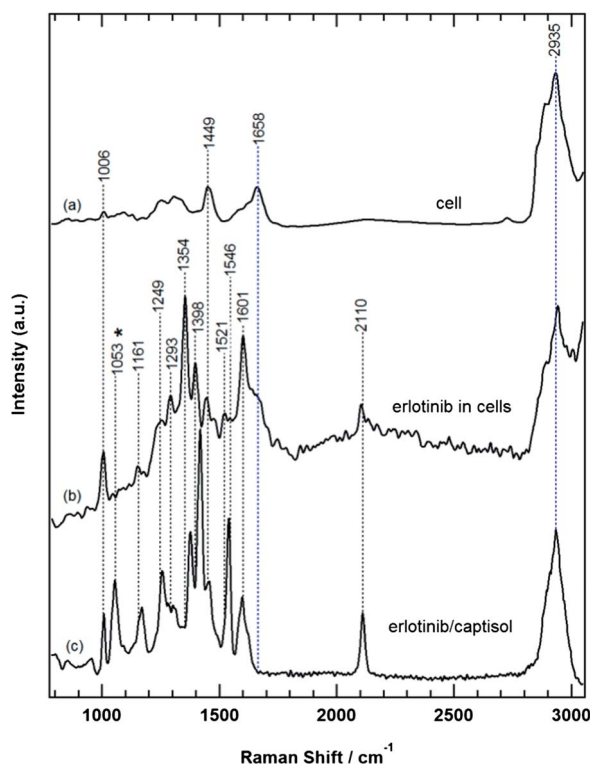

Fig. 2 Raman spectra of cells and erlotinib. (a) Average Raman spectrum of regions within cells lacking the drug, (b) average Raman spectrum of drug regions within cells, and (c) Raman spectrum of free erlotinib dissolved in 6% captisol as a carrier. The asterisk indicates the captisol band (see also Fig. S6 in the ESI†). The Raman signals at 2935 and 1658 cm^{-1} (blue) in the spectrum (b) arise from lipids and proteins in cells, respectively.
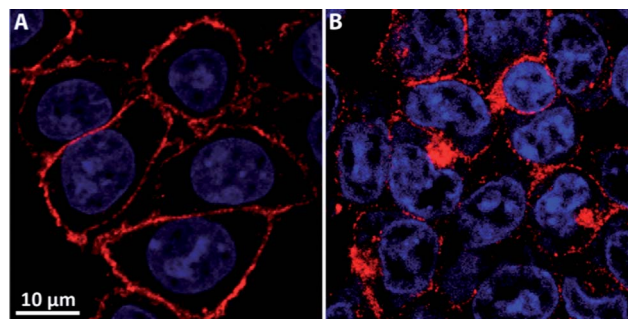

Fig. 3 Fluorescence imaging of SW480 cells. (A) Fluorescence imaging of SW480 cells (control). (B) Fluorescence imaging of SW480 cells in the presence of erlotinib. The nucleus and EGFR are shown in blue and red, respectively.

internalization of EGFR was observed in the absence of erlotinib, we suggest that the observed clustering of EGFR in SW480 cells can be explained in terms of EGFR internalization induced by erlotinib that inhibits the cell proliferation.[50]

Identification of an erlotinib metabolite

The metabolism of erlotinib has been investigated in humans and it was found that erlotinib is extensively metabolized by the cytochrome P450 (CYP) enzymes, mostly by CYP3A4 and CYP3A5 and to a lesser extent by CYP1A1 and CYP1A2, with metabolites primarily excreted by the biliary system.[51,52] There are three major routes to erlotinib metabolism, as shown in Scheme 1: O-demethylation (I) of the side chain with or without further oxidation to the carboxylic acid (II), oxidation of the acetylene moiety to the aryl carboxylic acid (III), and 4-hydroxylation of the phenyl-acetylene moiety (IV).[51] Since the C≡C vibrations are observed at 2110 cm^{-1} in the Raman spectrum (Fig. 2b), we exclude the oxidation of the acetylene moiety to the aryl carboxylic group (III) under our experimental conditions.

Another preserved marker band is that at 1006 cm^{-1}. It can be assigned to the trigonal ring deformation of the phenyl group. It is known that this strong band is only present in mono, 1,3-, and 1,3,5-substituted benzene derivatives.[53] Thus, it is found in erlotinib, where the phenyl group is 1,3 substituted, but upon 4-hydroxylation of the phenyl group (compound IV in Scheme 1), this band would disappear.[32] Since the band at 1006 cm^{-1} is still found in the spectrum of metabolized erlotinib (Fig. 2b), we can rule out this route. We were able to confirm this behaviour of the 1006 cm^{-1} band by quantum chemical calculations (see Fig. S2 in the ESI†). Thus, the observed metabolite in the present Raman study most likely originates from O-demethylation (I) of the side chain with or without further oxidation to the carboxylic acid (II).

To determine the exact metabolite structure, we performed Raman measurements of a synthetic metabolite standard, desmethyl-erlotinib (I), and the results are shown in Fig. 4. The spectrum of desmethyl-erlotinib (b) is almost identical to that of metabolized erlotinib observed in SW480 cells (a).

The only difference is that the spectrum (a) contains contributions from cellular components as explained above.
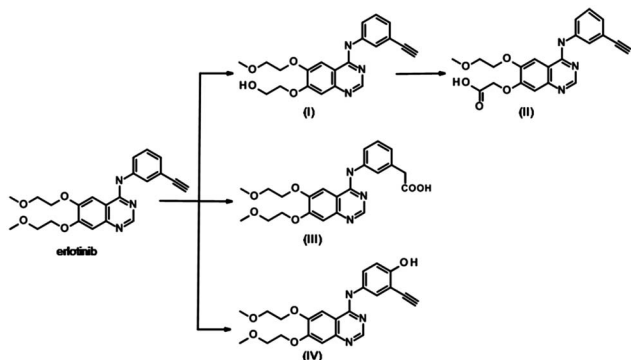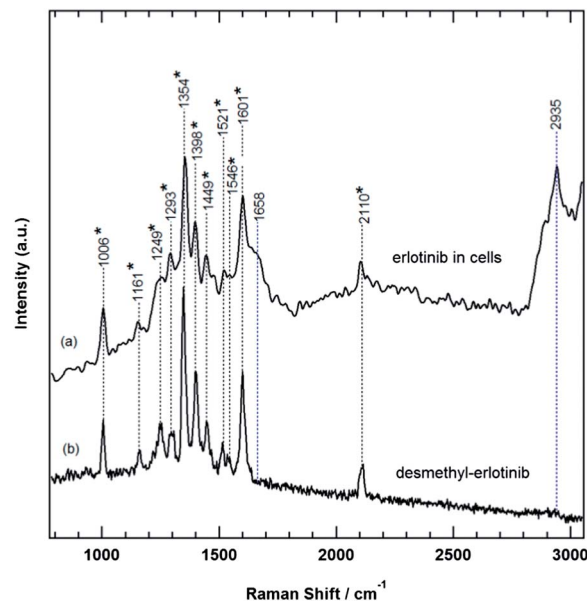

Fig. 4 Raman spectra of metabolized erlotinib in cells and desmethyl-erlotinib. (a) Average Raman spectrum of erlotinib regions within cells shown in Fig. 2b and (b) Raman spectrum of the synthetic metabolite standard desmethyl-erlotinib. The asterisks indicate the desmethyl-erlotinib bands in (a). The Raman signals at 2935 and 1658 cm^{-1} (blue) arise from lipids and proteins in the cells, respectively.

Therefore, Raman results indicate that the detected metabolite in SW480 cells is desmethyl-erlotinib. Although this metabolite was detected previously by liquid chromatography tandem mass spectrometry, high-pressure liquid chromatography mass spectrometry, and MALDI-MS in human plasma and rat tissue sections,[5,54,55] this is the first report of its detection and spatially resolved allocation within cells using the label-free technique of Raman vibrational microscopy.

The detected concentrations of erlotinib and desmethyl-erlotinib metabolite in human plasma of patients after the orally recommended dose of 150 mg per day were found to be 3–5 μM and 0.2–0.7 μM, respectively.[54,56] These concentrations are too low to be detected by conventional Raman spectroscopy because of weak signals of Raman scattering, which led to use of higher erlotinib concentration in the present study.

There are several ways to detect low concentration by Raman microscopy. For instance, surface enhanced Raman[57] or a nonlinear technique such as stimulated Raman scattering (SRS)[14] can be used due to its strong Raman signals. SRS imaging of drug distribution and metabolism is our next project.

Conclusions

Raman microscopy resolves the subcellular organelles and shows the spatial distribution and metabolism of molecular target agent erlotinib within colon cancer cells. This study provides new insights into the mechanisms of drug uptake and intracellular targeting. In addition, it demonstrates the potential of Raman microscopy as a non-invasive and label-free technique to investigate pharmacokinetics.

Scheme 1 Proposed metabolic scheme of the biotransformation of erlotinib.

Acknowledgements

Notes and references

1 H. Su, C. Bodenstein, R. A. Dumont, Y. Seimbille, S. Dubinett, M. E. Phelps, H. Herschman, J. Czernin and W. Weber, *Clin. Cancer Res.*, 2006, **12**, 5659–5667.

2 E. G. Solon, S. K. Balani and F. W. Lee, *Curr. Drug Metab.*, 2002, **3**, 451–462.

3 N. Beckmann, D. Laurent, B. Tigani, R. Panizzutti and M. Rudin, *Drug Discovery Today*, 2004, **9**, 35–42.

4 R. M. Caprioli, T. B. Farmer and J. Gile, *Anal. Chem.*, 1997, **69**, 4751–4760.

5 L. Signor, E. Varesio, R. F. Staack, V. Starke, W. F. Richter and G. Hopfgartner, *J. Mass Spectrom.*, 2007, **42**, 900–909.

6 F. J. Troendle, C. D. Reddick and R. A. Yost, *J. Am. Soc. Mass Spectrom.*, 1999, **10**, 1315–1321.

7 G. Marko-Varga, T. E. Fehniger, M. Rezeli, B. Döme, T. Laurell and A. Végvári, *J. Proteomics*, 2011, **74**, 982–992.

8 J. Popp, *Handbook of biophotonics. Volume 2, Photonics for health care*, Wiley-VCH, John Wiley [distributor], Weinheim, Chichester, 2011.

9 C. Matthäus, T. Chernenko, J. A. Newmark, C. M. Warner and M. Diem, *Biophys. J.*, 2007, **93**, 668–673.

10 C. Krafft, T. Knetschke, R. H. W. Funk and R. Salzer, *Anal. Chem.*, 2006, **78**, 4424–4429.

11 H.-J. van Manen, *Proc. Natl. Acad. Sci. U. S. A.*, 2005, **102**, 10159–10164.

12 C. Matthäus, S. Boydston-White, M. Miljković, M. Romeo and M. Diem, *Appl. Spectrosc.*, 2006, **60**, 1–8.

13 N. Uzunbajakava, A. Lenferink, Y. Kraan, E. Volokhina, G. Vrensen, J. Greve and C. Otto, *Biophys. J.*, 2003, **84**, 3968–3981.

14 B. G. Saar, C. W. Freudiger, J. Reichman, C. M. Stanley, G. R. Holtom and X. S. Xie, *Science*, 2010, **330**, 1368–1370.

15 M. E. Keating and H. J. Byrne, *Nanomedicine*, 2013, **8**, 1335–1351.

16 C. Matthäus, A. Kale, T. Chernenko, V. Torchilin and M. Diem, *Mol. Pharm.*, 2008, **5**, 287–293.

17 T. Chernenko, R. R. Sawant, M. Miljkovic, L. Quintero, M. Diem and V. Torchilin, *Mol. Pharm.*, 2012, **9**, 930–936.

18 J. Dorney, F. Bonnier, A. Garcia, A. Casey, G. Chambers and H. J. Byrne, *Analyst*, 2012, **137**, 1111–1119.

19 H. Yamakoshi, K. Dodo, M. Okada, J. Ando, A. Palonpon, K. Fujita, S. Kawata and M. Sodeoka, *J. Am. Chem. Soc.*, 2011, **133**, 6102–6105.

20 J. Ling, S. D. Weitman, M. A. Miller, R. V. Moore and A. C. Bovik, *Appl. Opt.*, 2002, **41**, 6006.

21 A. V. Feofanov, A. I. Grichine, L. A. Shitova, T. A. Karmakova, R. I. Yakubovskaya, M. Egret-Charlier and P. Vigny, *Biophys. J.*, 2000, **78**, 499–512.

22 Y. Harada, P. Dai, Y. Yamaoka, M. Ogawa, H. Tanaka, K. Nosaka, K. Akaji and T. Takamatsu, *Histochem. Cell Biol.*, 2009, **132**, 39–46.

23 H. Salehi, L. Derely, A.-G. Vegh, J.-C. Durand, C. Gergely, C. Larroque, M.-A. Fauroux and F. J. G. Cuisinier, *Appl. Phys. Lett.*, 2013, **102**, 113701.

24 K. Meister, J. Niesel, U. Schatzschneider, N. Metzler-Nolte, D. A. Schmidt and M. Havenith, *Angew. Chem., Int. Ed. Engl.*, 2010, **49**, 3310–3312.

25 A. Arora and E. M. Scholar, *J. Pharmacol. Exp. Ther.*, 2005, **315**, 971–979.

26 B. Fischer, M. Marinov and A. Arcaro, *Cancer Treat. Rev.*, 2007, **33**, 391–406.

27 B. Pajares, E. Torres, J. M. Trigo, M. I. Sáez, N. Ribelles, B. Jiménez and E. Alba, *Clin. Transl. Oncol. Off. Publ. Fed. Span. Oncol. Soc. Natl. Cancer Inst. Mex.*, 2012, **14**, 94–101.

28 G. Manning, D. B. Whyte, R. Martinez, T. Hunter and S. Sudarsanam, *Science*, 2002, **298**, 1912–1934.

29 P. Traxler and P. Furet, *Pharmacol. Ther.*, 1999, **82**, 195–206.

30 J. S. Sebolt-Leopold and J. M. English, *Nature*, 2006, **441**, 457–462.

31 J. Zhang, P. L. Yang and N. S. Gray, *Nat. Rev. Cancer*, 2009, **9**, 28–39.

32 D. R. Duckett and M. D. Cameron, *Expert Opin. Drug Metab. Toxicol.*, 2010, **6**, 1175–1193.

33 R. Pazdur, *Cancer management: a multidisciplinary approach: medical, surgical, & radiation oncology*, Oncology Group, New York, 2003.

34 J. Mendelsohn, *J. Clin. Oncol.*, 2003, **21**, 2787–2799.

35 T. M. Brand, M. Iida, C. Li and D. L. Wheeler, *Discov. Med.*, 2011, **12**, 419–432.

36 L. Mavarani, D. Petersen, S. F. El-Mashtoly, A. Mosig, A. Tannapfel, C. Kötting and K. Gerwert, *Analyst*, 2013, **138**, 4035.

37 V. J. Stella and Q. He, *Toxicol. Pathol.*, 2008, **36**, 30–42.

38 T. Friess, W. Scheuer and M. Hasmann, *Clin. Cancer Res. off. Off. J. Am. Assoc. Cancer Res.*, 2005, **11**, 5300–5309.

39 M. Miljković, T. Chernenko, M. J. Romeo, B. Bird, C. Matthäus and M. Diem, *Analyst*, 2010, **135**, 2002.

40 I. I. Patel, J. Trevisan, G. Evans, V. Llabjani, P. L. Martin-Hirsch, H. F. Stringfellow and F. L. Martin, *Analyst*, 2011, **136**, 4950.

41 R. Salzer, *Infrared and Raman spectroscopic imaging*, Wiley-VCH, Weinheim, 2009.

42 J. R. Lakowicz, *Principles of fluorescence spectroscopy*, Springer, New York, N.Y., 2006.

43 J. D. Moyer, E. G. Barbacci, K. K. Iwata, L. Arnold, B. Boman, A. Cunningham, C. DiOrio, J. Doty, M. J. Morin, M. P. Moyer, M. Neveu, V. A. Pollack, L. R. Pustilnik, M. M. Reynolds, D. Sloan, A. Theleman and P. Miller, *Cancer Res.*, 1997, **57**, 4838–4848.

44 A. Huether, M. Höpfner, A. P. Sutter, D. Schuppan and H. Scherübl, *J. Hepatol.*, 2005, **43**, 661–669.

45 F. Yamasaki, D. Zhang, C. Bartholomeusz, T. Sudo, G. N. Hortobagyi, K. Kurisu and N. T. Ueno, *Mol. Cancer Ther.*, 2007, **6**, 2168–2177.

46 Y.-H. Ling, T. Li, Z. Yuan, M. Haigentz, T. K. Weber and R. Perez-Soler, *Mol. Pharmacol.*, 2007, **72**, 248–258.

47 S. Bhattacharyya, R. Bhattacharya, S. Curley, M. A. McNiven and P. Mukherjee, *Proc. Natl. Acad. Sci. U. S. A.*, 2010, **107**, 14541–14546.

48 H. Sunada, B. E. Magun, J. Mendelsohn and C. L. MacLeod, *Proc. Natl. Acad. Sci. U. S. A.*, 1986, **83**, 3825–3829.

49 J. F. Doody, Y. Wang, S. N. Patel, C. Joynes, S. P. Lee, J. Gerlak, R. L. Rolser, Y. Li, P. Steiner, R. Bassi, D. J. Hicklin and Y. R. Hadari, *Mol. Cancer Ther.*, 2007, **6**, 2642–2651.

50 W.-L. Yeo, G. J. Riely, B. Y. Yeap, M. W. Lau, J. L. Warner, K. Bodio, M. S. Huberman, M. G. Kris, D. G. Tenen, W. Pao, S. Kobayashi and D. B. Costa, *J. Thorac. Oncol.*, 2010, 1.

51 J. Ling, K. A. Johnson, Z. Miao, A. Rakhit, M. P. Pantze, M. Hamilton, B. L. Lum and C. Prakash, *Drug Metab. Dispos. Biol. Fate Chem.*, 2006, **34**, 420–426.

52 J. Li, M. Zhao, P. He, M. Hidalgo and S. D. Baker, *Clin. Cancer Res. Off. J. Am. Assoc. Cancer Res.*, 2007, **13**, 3731–3737.

53 F. A. Miller, *J. Raman Spectrosc.*, 1988, **19**, 219–221.

54 A. R. Masters, C. J. Sweeney and D. R. Jones, *J. Chromatogr. B: Anal. Technol. Biomed. Life Sci.*, 2007, **848**, 379–383.

55 M. Zhao, P. He, M. A. Rudek, M. Hidalgo and S. D. Baker, *J. Chromatogr. B: Anal. Technol. Biomed. Life Sci.*, 2003, **793**, 413–420.

56 M. Hidalgo, L. L. Siu, J. Nemunaitis, J. Rizzo, L. A. Hammond, C. Takimoto, S. G. Eckhardt, A. Tolcher, C. D. Britten, L. Denis, K. Ferrante, D. D. Von Hoff, S. Silberman and E. K. Rowinsky, *J. Clin. Oncol.*, 2001, **19**, 3267–3279.

57 S. Schlücker, *Surface enhanced Raman spectroscopy: analytical, biophysical and life science applications*, Wiley-VCH Verlag, Weinheim, Germany, 2011.